

Galactic seismology: can a disc-crossing impulse explain the large-scale perturbations in the Milky Way's disc?

Pavadol Yamsiri,¹★ Joss Bland-Hawthorn¹ and Thor Tepper-Garcia¹

¹Sydney Institute for Astronomy, School of Physics, A28, The University of Sydney, Sydney, NSW 2006, Australia

Last updated YYYY MM DD; in original form YYYY MM DD

arXiv:2602.05296v1 [astro-ph.GA] 5 Feb 2026

ABSTRACT

Prior to its infall, the Sagittarius (Sgr) dwarf galaxy was a major satellite with a mass of $M_{\text{sgr}} \sim 10^{11} \text{ M}_{\odot}$. For the past 5 – 6 Gyr, it has been heavily stripped by the Milky Way (MW), losing most of its mass while crossing the MW disc multiple times. Recent models of Milky Way disc perturbations – including the spiral arms, the stellar bar, the *Gaia* phase spiral, and stellar and gaseous disc corrugations – have identified these crossings as possible formation triggers, but have generally treated each perturbation in isolation. Here, we adopt a holistic perspective and ask whether a single disc-crossing impulse can simultaneously account for these features as observed today. We focus on simulations of single disc-crossing events by a Sgr-like perturber, and present a forensic analysis of the role of the powerful impulse in forming spiral arms, disc corrugations, the phase spiral and the ' $L_z - \bar{V}_R$ wave', determined from a star's angular momentum and radial velocity, respectively. We find that a single disc crossing can reproduce reasonably well (e.g. structure, amplitude, phase) the observed local disc corrugation, and the Outer, Local and Sagittarius-Carina arm segments, implying that the last significant impulse due to a transit took place 700 – 1200 Myr ago. Moreover, the $L_z - \bar{V}_R$ wave and phase spiral appear within the simulations over the same epoch and their general structure is reasonably well replicated, but not in detail. We conclude that Sgr's last significant crossing roughly a Gyr ago could be the primary cause of large-scale MW disc perturbations, but it cannot fully account for the $L_z - \bar{V}_R$ wave. Consequently, other triggers, possibly the Galactic bar or interactions with other satellites, must be considered in order to fully explain the current dynamical state of the MW's disc.

Key words: galaxies: kinematics and dynamics - Galaxies methods: numerical - software: simulations

1 INTRODUCTION

The advent of the European Space Agency (ESA) *Gaia* astrometric mission and its major data releases has led to the discovery of many phase space¹ substructures in the Milky Way stellar disc. These features include ridges seen in $R - V_{\phi}$ (Antoja et al. 2018; Monari et al. 2017), spirals in vertical phase space $z - V_z$ known as *phase spirals* (Antoja et al. 2018), planar waves seen in V_R (Friske & Schönrich 2019) and many more. Such substructures are evidence that the Milky Way (MW) is in the process of settling from a perturbed state in the recent past. In particular, the phase spiral, which appears as a one-arm spiral pattern in the vertical phase-space distribution $z - V_z$ of stars in the local Solar neighbourhood, is likely the result of phase mixing (Lynden-Bell 1967) after a strong impulsive disturbance of the disc. Potential sources of these perturbations could be satellite galaxies like Sagittarius (Sgr), bar buckling (Khoperskov et al. 2019), dark matter wakes induced by satellites (Grand et al. 2023), or a series of stochastic kicks by objects like molecular clouds or dark matter subhalos (Tremaine et al. 2023).

The MW disc has also been shown to be corrugated, displaying both small-scale, wave-like oscillations from the local disc (Widrow

et al. 2012; Bennett & Bovy 2019) all the way to the outer disc, coexisting with the outer warp (Schönrich & Dehnen 2018). In particular, Bennett & Bovy (2019) showed that the local vertical asymmetry was found across various stellar colours and ages and that they were consistent, indicating a single shared origin, such as from a single perturbation event (see also Poggio et al. 2025). Corrugations are seen in high-resolution simulations of disc-satellite interactions (Purcell et al. 2011; Antoja et al. 2022). Notably, Bland-Hawthorn & Tepper-García (2021) first showed that an impulse-triggered corrugation (bending mode) winds up like the associated spiral density wave, but at half the angular rate.

Spiral arms are a common feature of almost all disc galaxies. The MW spiral arms have been observed across different tracers, such as masers shown in studies by Reid et al. (2014) and Reid et al. (2019), stars through surveys like *Gaia* by Poggio et al. (2021) and also in gas (q.v. Söding et al. 2025). For many decades, the origin of spiral arms and their exact nature have been under constant debate with theories ranging from eternal and static density waves (Lin & Shu 1964), now discredited, and transient structures popping in and out of existence (Sellwood & Carlberg 1984). Spiral arms can arise from various mechanisms, including swing-amplified instabilities, bar-induced or tidally-induced excitations, or self-excited disc modes (Purcell et al. 2011; Sellwood & Carlberg 2022).

Thus the MW is host to many asymmetries that are plausibly explained by a tidal interaction with an external perturber such as

★ Email: pyam4330@uni.sydney.edu.au

¹ In Galactic cylindrical coordinates (R, ϕ, z), individual stars have velocities (V_R, V_{ϕ}, V_z) and oscillation frequencies ($\Omega_R, \Omega_{\phi}, \Omega_z$) = (κ, Ω, ν).

the Sgr dwarf. However it is still unclear how dominant are recent pericentric passage of Sgr to the current structure and state of the MW. [Bland-Hawthorn & Tepper-García \(2021\)](#) have shown that a single satellite disc crossing can incite both in-plane spiral density waves and vertical bending waves. These waves do not only rotate but also wrap over time leading to increasingly wrapped spiral arms and corrugations respectively. The angular wrapping rates of such waves differ with the bending wave wrapping slower than the spiral density wave, such that spiral arms oscillate in height over azimuth as opposed to being confined to the plane. This mechanism is proposed to be the most likely origin of the coupling between the vertical phase spiral seen in mass density and its in-plane motion encoded by the mean radial velocity $\langle V_R \rangle$ and the mean azimuthal velocity $\langle V_\phi \rangle$.

This link and relationship between these tidally-induced spiral arms, the disc corrugation and the phase spiral could serve as an explanation as to how these features originated in the MW itself via a single shared origin.

This study aims to test this mechanism by further examining the N-body simulation used in [Bland-Hawthorn & Tepper-García \(2021\)](#), along with more advanced models, to investigate the plausibility of such an origin; that the last significant crossing of Sgr is responsible for the current spiral structure, corrugated disc and phase spirals in the modern MW. Included in our consideration is the condition that such MW-like features must also be consistent with each other, meaning that they are observed from the same point in time and space in the simulation.

The paper is set out in the following way: the experimental setup is given in Sec. 2, the overall strategy in Sec. 3 followed by the results in Sec. 4. Sec. 5 will discuss how the addition of gas and more advanced gas physics will affect our results and finally in Sec. 6 we will summarise our findings.

2 EXPERIMENTAL SETUP

We evaluate the plausibility of such a model by looking at an isolated galactic disc simulation, first presented in [Bland-Hawthorn & Tepper-García \(2021\)](#) (hereafter referred to as **BT21**). In this model, the MW is approximated by a three component system, which consists of: 1) a dark matter (DM) halo; 2) a pre-assembled stellar bulge; and 3) a pre-assembled stellar disc. The three components are all responsive, and they are sampled with 2×10^7 particles (DM halo), and 4.5×10^6 particles (stellar bulge), and 5×10^7 particles (stellar disc). The masses of the three components are approximately $1.4 \times 10^{12} M_\odot$, $1.5 \times 10^{10} M_\odot$, and $3.4 \times 10^{10} M_\odot$, respectively.

The simulations have been carried out with the **NEXUS** framework ([Tepper-García et al. 2024](#)). In brief, the initial conditions for each galaxy component were created using the Action-based Galaxy Modelling Architecture (AGAMA) stellar dynamics library ([Vasiliev 2019](#)), which have been complemented to include gas in addition to the standard treatment of collisionless components.

The initial conditions are evolved with the adaptive mesh refinement (AMR), N-body/hydrodynamical code **RAMSES** ([Teyssier 2002](#)), augmented with a proprietary module to account for galaxy formation physics (q.v. [Agertz et al. 2021](#)).

In order to keep the disc reasonably stable against the development of instabilities from the outset, we choose the stellar radial velocity dispersion σ_R such that Toomre's stability parameter defined by

$$Q_* \equiv \frac{\sigma_R \kappa}{3.36 G \Sigma_*} \quad (1)$$

where κ is the epicyclic frequency and Σ_* is the stellar surface density, is above 1.3 across the disc. As a result of the the relatively low disc

mass fraction, the model galaxy is stable against the bar-instability over at least 4 Gyr ([Fujii et al. 2018; Bland-Hawthorn et al. 2023](#)).

Originally, **BT21**'s model was designed to mimic the analytic toy model presented by [Binney & Schönrich \(2018\)](#), in which the Sagittarius dwarf galaxy (Sgr) is approximated by a point mass. Its orbital parameters are such that it intersects the galactic midplane of the disc at $R \approx 18$ kpc travelling at an infall speed of 330 km s^{-1} .

In order to isolate the effects of a single impact, the mass of the perturber is artificially reduced over time. The mass evolves as follows

$$M_P(t) = M_P(0) \times \begin{cases} 1 & t < t_0 \\ \exp\left(\frac{-(t-t_0)}{\tau_s}\right) & t \geq t_0 \end{cases} \quad (2)$$

where $M_P(0) = 2 \times 10^{10} M_\odot$ and $\tau_s = 30 \text{ Myr}$, roughly a disc crossing time. The perturber first crosses the disc at about $\sim 100 \text{ Myr}$ and so t_0 is set to 150 Myr. This mass loss means that at the perturber's second disc crossing, its mass becomes negligible. Hence, this model serves as a useful proxy for exploring the effects of a "Sagittarius dwarf"-sized impact onto the Milky Way disc.²

3 METHODS

The main goal of this study is to explore whether a single, impulsive interaction between Sgr and the MW can account for the large-scale perturbation of the Milky Way disc we observe today. We do this by comparing on a like-for-like basis the perturbations of the synthetic galaxy in **BT21**'s model with MW data, and quantifying their similarities and differences. The details of our approach are presented and discussed in the following sections.

3.1 Reference Frame

All observations and measurements of the MW's structure are carried out in a heliocentric frame, while our simulations are effectively ran in a Galactocentric frame. A meaningful comparison between observations and simulations requires them to be in the same frame of reference; we choose for this purpose the heliocentric frame and thus map all of our simulation results to this frame, as explained next.

We adopt a Sun to Galactic centre distance of $R_0 = 8 \text{ kpc}$ and a Sun to midplane height of $z_0 = 0 \text{ kpc}$ to simplify the coordinate transformations.³

In a synthetic MW disc featuring a central stellar bar, there are two possible and fully equivalent sun positions, each at a location (R_0, z_0) and at an angle of roughly 28° with respect to either bar end (see e.g. [Tepper-García et al. 2021](#), their figure 3). In contrast, in an perfectly axisymmetric disc - as is the case of our adopted model - there is no preference for any azimuth. Therefore, any location on a circle with radius equal to R_0 - the solar circle - is a valid reference point to compare with observation, creating a circle of candidate reference frames.

See Fig. 1 for a diagram of the reference points around the solar circle (inner white circle), and their respective selection regions (to be introduced in the following sections).

² We refer the reader to **BT21** for a more detailed account and description of the simulation.

³ This does make some comparisons with observations inconsistent as for example the spiral arms assume a different Galactocentric frame. This does not significantly change the results.

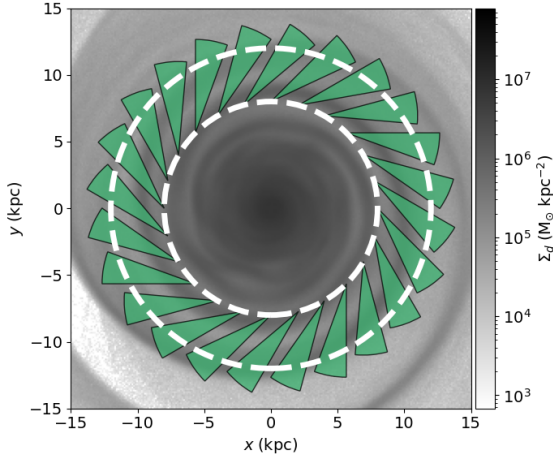


Figure 1. Illustration of 24 wedge shaped selections shaded in green used to sample the radial height profile or *corrugation*, overlaid on top of a synthetic galactic disc that is rotating anti-clockwise. In addition to the wedge shaped selection there are further cuts on Galactocentric radius denoted by the inner and outer dashed white circles. The selection is an approximation of the projected selection used by Yin & Hinkel (2024) in their analysis of the local radial height profile. Note that only 24 of the 72 wedges we used for our analysis are shown here to avoid excessive visual clutter. See Sec. 3.4 for a more detailed description of this selection.

3.2 General Strategy

In order to quantify the correspondence between the simulated and the observed perturbations inflicted upon the MW’s stellar disc we introduce hereafter a ‘similarity’ metric individually for each corresponding feature: spiral arms, corrugation, phase spiral, and $L_z - \bar{V}_R$ wave

Given our choice of reference frame (Sec. 3.1), we apply each metric for 72 locations, i.e. azimuths, around the solar circle (cf. Fig. 1, green shaded regions), and for a range of time steps over the full evolution of the system after impact.

For each feature, this results in a two-dimensional (2D) map in time (across snapshots) and in azimuth (along the solar circle) where the map value at each cell indicates the similarity between simulation and data, allowing for a visual assessment of the epoch and azimuth pairs at which the simulation provides a reasonable match to observations.

3.3 Spiral Arms

3.3.1 Observation

To quantify the correspondence between simulation and observations with regards to the presence and structure of the stellar spiral arms, we use a spiral arm model adapted from Reid et al. (2019, see their Table 2). The adopted models consist of arc segments *interpolated* across the locations of masers to limit the bias towards any particular spiral arm model. This means we do not adopt the full spiral arm model as shown in Fig. 1 of Reid et al. (2019) as that involved extrapolating fitted arm segments beyond their observed sources. Specifically, we consider the *Scutum-Centauri*, *Sagittarius-Carina*, *Local*, *Perseus* and *Outer* arm segments, excluding the two innermost arms, the 3-kpc(N) and Norma arms appear too close to the Galactic bar, which is missing in the simulations considered in this report.

The spiral arm segments are modelled as kinked log spirals de-

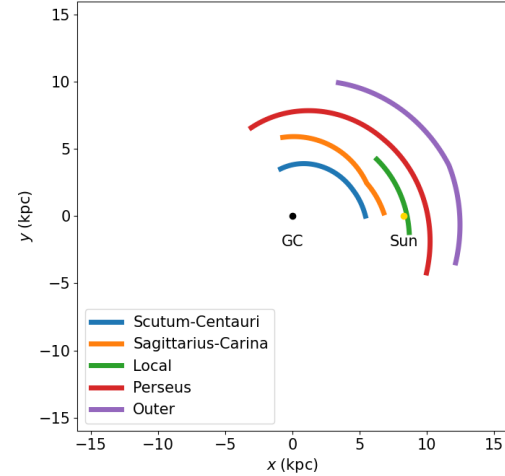


Figure 2. Spiral arm segments adapted from Reid et al. (2019), shown as they would appear if the Sun were located at $(X, Y) = (8, 0)$ kpc and the disc rotated anti-clockwise. Note that we do not use the four arm plus Local arm model proposed by Reid et al. (2019) which extrapolated fitted arm segments instead plotting the arm segments only across the azimuths where maser sources are observed using the parameters seen in Table 2. The innermost arms, the 3 kpc(N) and Norma arms are excluded, since they exist too close to the Galactic bar which is not included in the simulations considered in this study.

scribed by the following functional form

$$\ln \left(\frac{R}{R_{\text{kink}}} \right) = -(\beta - \beta_{\text{kink}}) \tan \psi_{\pm} \quad (3)$$

where R is the Galactocentric radius and β is the azimuth defined as 0 towards the Sun and increasing in the direction of Galactic rotation. The arm is then parametrised by the following parameters: R_{kink} is the kink radius, β_{kink} is the kink azimuth and ψ_{\pm} are pitch angles which can differ depending on whether β is larger or smaller than β_{kink} .

We refer the reader to Fig. 2 for a sketch of the adopted arm segments and their relative position to the Sun.

3.3.2 Simulation

As explained in Sec. 3.3.1, our adopted spiral arms are modelled in terms of a Galactocentric frame where the Sun is assumed to be at $R = R_{\odot} = 8$ kpc, $\phi = 0$ and $z = z_{\odot} = 0$ kpc. Therefore, for each possible location along the solar circle we have a continuous spectrum of possible positions of the spiral arms. We then need to evaluate for each position how well the simulation reproduces the MW spiral arms.

3.3.3 Comparison

The similarity metric we will use for the spiral arms is based on a spatial ‘mask-based’ approach. In essence, we discretise the arms into pixel masks over a 2D Cartesian grid projection of the disc’s stellar surface density in the $x - y$ plane. Each mask identifies the region associated with a particular arm segment. We compute the number of pixels within each mask that are classified as ‘overdense’, and divide that by the total number of pixels contained within the mask. ‘Overdense’ cells are those with a higher stellar surface density

relative to the initial surface density when the disc was smooth, i.e. at the beginning ($t = 0$) of the simulation.

The overdensity Δ is defined as follows

$$\Delta(x, y, t) = \frac{\Sigma(x, y, t)}{\Sigma(x, y, 0)} \quad (4)$$

where $\Sigma(x, y, z, t)$ is the stellar surface density at point x, y at time t . An overdense cell is then a cell where this quantity is greater than 1.

The spiral arm similarity metric is then defined as follows

$$S_{\text{arm}} = \frac{\# \text{ of overdense cells within mask}}{\# \text{ of total cells within mask}} \quad (5)$$

This metric represents the fraction of overdense cells falling within a particular arm segment region serving as a proxy for how well the simulated spiral arms are aligned with the observed spiral arms. Its value ranges from 0, which indicates poor correspondence, to 1, which implies perfect correspondence. We note that in principle a value of 1 does not actually mean perfect alignment as one can one can imagine a disc with large overdense regions that fall within the masks but do not form spiral arm segments resembling the given spiral arm models (see Appendix A for a more in-depth explanation). However, for the simulations studied in this work, this effect is not that significant, as the overdensity map is a reasonable proxy for the locating spiral arms.

3.4 Corrugation

Disc corrugations tend to span entire galactic discs (see Fig. 21 in Bland-Hawthorn et al. 2019). However, reliable measurements in *Gaia* trace only the local disc, in part due to dust but also due to our position within the MW itself (Poggio et al. 2025). Observationally, we can really only sample part of the disc to a high degree of confidence. It is therefore not possible to compare the global structure of disc corrugations between observations and simulations. Thus, we must settle for proxies of the global disc corrugation in the form of local trends in the height of the midplane.

3.4.1 Observation

In a paper by Yin & Hinkel (2024) they have shown the presence of a radial wave in height in a wedge shaped region centred on the Sun.

Their selection can be summarised as follows:

- (i) a cut in parallax $p \geq 0$
- (ii) a cut in G band apparent magnitude $G_{\text{mag}} \in [13, 18]$ mag
- (iii) a cut in *Gaia* colour $G_{\text{BP}} - G_{\text{RP}} \in [0.6, 2.4]$
- (iv) a cut in Galactic longitude $l \in [225, 245]$ $^{\circ}$
- (v) a cut⁴ given by

$$3.8857 G_{\text{BPRP}} - 0.4312 \leq M_G \leq 3.4251 G_{\text{BPRP}} + 1.517 \quad (6)$$

where

$$M_G = G_{\text{mag}} - 5 \log_{10} \left(\frac{d}{10 \text{ pc}} \right) \quad (7)$$

is the absolute G band magnitude and

$$G_{\text{BPRP}} = G_{\text{BP}} - G_{\text{RP}} \quad (8)$$

is the difference between G band magnitudes.

⁴ this cut was not mentioned in Yin & Hinkel (2024), however, it was used to obtain their results (confirmed via private communication).

The selected stars are then binned radially from 8 to 12 kpc and the stars in each radial bin are then binned again in height. See the green shaded regions in Fig. 1 for examples of the shape of the selection.

The height distribution in each radial bin is passed through an odd low-pass filter to remove any long wavelength odd oscillations and the mean height of the resulting distribution is taken to be the mean height of the plane for that bin. The odd low pass filter works as follows:

$$\begin{aligned} & \text{(i) Take the Fourier transform of a spatial distribution } \psi \\ & \psi(x) \rightarrow \psi(\tilde{v}) \end{aligned} \quad (9)$$

where x is the spatial coordinate and \tilde{v} is the linear wavenumber.

(ii) For wavenumbers greater than some set limit $\tilde{v} > \tilde{v}_{\text{lim}}$, ignore the imaginary component or more specifically apply the following function $F(\tilde{v})$

$$F(\tilde{v})\psi(\tilde{v}) = \begin{cases} \psi(\tilde{v}) & \tilde{v} \leq \tilde{v}_{\text{lim}} \\ \Re(\psi(\tilde{v})) & \tilde{v} > \tilde{v}_{\text{lim}} \end{cases} \quad (10)$$

where $\Re(x)$ returns the real part of x .

(iii) The resulting distribution in frequency space is converted back into the spatial domain to retrieve the filtered distribution.

We adopt the same frequency cutoff $\tilde{v} = 0.5 \text{ kpc}^{-1}$ as Yin & Hinkel (2024).

3.4.2 Simulation

The selection function described in the previous section barring cuts on stellar parameters like magnitude and colour can be replicated in our simulations allowing for a direct comparison between the radial waves in the simulations and the wave observed by Yin & Hinkel (2024).

In addition to the selection function we add uncertainty to the radial distances to each star with respect to the reference point to mimic the observational distance errors and make the comparison more fair. The inclusion of distance errors is motivated by Hey et al. (2023) who have demonstrated that uncertainty in distance can greatly influence observables. For simplicity, distances are sampled from a distribution where the mean is its true value and its half width at half maximum is equal to 15% of its true value.

3.4.3 Comparison

We aim to show that galaxy models with a single impulse can reproduce the corrugation. This requires a metric with which to quantify how much the simulation's radial wave resembles the observations in order to conclude that the simulation can “reproduce” the corrugation.

There are a few properties we would like the metric to have:

- (i) The value ranges from 0 representing infinite dissimilarity and 1 representing that the two waves are identical.
- (ii) There is an intuitive interpretation of the values in between.

Both criteria can be achieved if we have a method of calculating distance between the simulated wave and the observed wave using the following equation

$$\text{similarity} = 1 - \frac{\text{distance}}{\text{distance} + \text{threshold}} \quad (11)$$

where distance is any arbitrary quantity that ranges from 0 meaning identical waves and infinity meaning infinite dissimilarity and

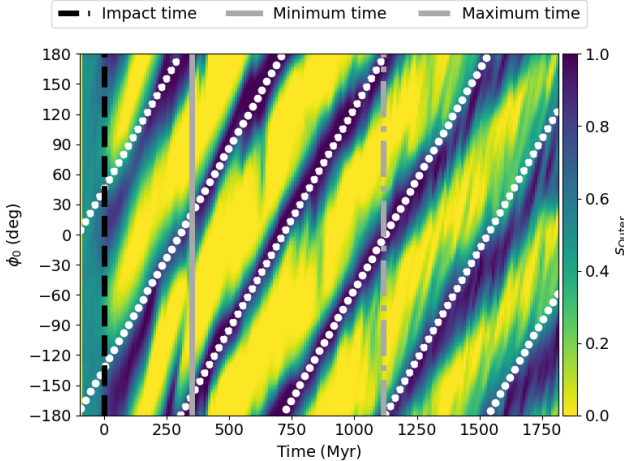


Figure 3. The arm coverage similarity of the Outer arm. The time is set relative to the time of impact and the azimuth is relative to the impact's azimuth, with positive azimuths going in the anti-clockwise direction in the direction of Galactic rotation. The impact time is outlined in black. High arm coverage is coloured dark blue whereas low arm coverage is coloured in yellow. The arm coverage is structured into diagonal bands that wrap in azimuth. The minimum time and maximum time refer to the range in time where the bands appear the most linear. A fit of the diagonal bands is also overlaid on top.

threshold refers to a threshold distance with which we want to compare to. For example, the threshold could be the distance between the observed wave and a wave resulting from a null model such as a galaxy model without an impact.

The result of Eqn. 11 is a similarity metric where a value of 0.5 means the current test wave is as similar to the observed wave as the null model. This then provides a natural threshold for determining if the simulations are able to produce radial waves that better match the observed corrugation compared to a null model. The null model in the case of the corrugation is that of a flat disc and so we use the distance between the observed wave and a flat profile with height equal to the mean height of the observed wave across all radial bins which is ~ 8 pc.

The distance score we will use from hereon is given by

$$NSSR = \sum_{i=1}^n \frac{(z_i - \hat{z}_i)^2}{\sigma_{z,i}^2 + \sigma_{\hat{z},i}^2} \quad (12)$$

which is simply the sum of square residuals each normalised by their combined variance. See Appendix B for a more in-depth discussion of how this residual-based similarity metric is sensitive to the signals like the corrugation.

4 RESULTS

4.1 Spiral Arms

In order to simplify the analysis of the spiral arms, we will limit to considering only the Outer arm at first. Using the mask-based similarity (from here on called the arm coverage), we construct a map of the similarity across time since impact and azimuth relative to the impact site's azimuth, which can be seen in Fig. 3.

The arm coverage map displays remarkable distinct bands. This indicates that the spiral arm segments in the simulation do resemble

the observed spiral arms and that they are rotating with the disc (see Appendix A for an explanation why). Soon after the impact the bands are formed and become highly resolved aside from a few kinks, but over time the bands' similarity starts to bleed out to other azimuths.

This is a result of the impact inciting a large-scale density wave that rotates with the disc. Over time the wave becomes increasingly wrapped from the centre outwards. At late times, this wrapping is so severe it causes the spiral wave to decohere due to diffusion between the wrappings of the arm, leading to the wispy nature of the high similarity bands in Fig. 3 later on. The evolution of the spiral density wave is illustrated in Fig. 4.

The same method to create Fig. 3 was used on the other four arm segments resulting in Fig. 5. It is apparent that arm segments with smaller average radii (Scutum-Centauri and Sagittarius-Centauri) tend to have their similarity bands decohere faster than arm segments with larger average radii (Local, Perseus and Outer). This reflects that the spiral density wave diffuses from inside out.

The diagonal bands can be modelled as rotating at a constant angular speed

$$\phi(t) = \Omega t + \phi_0 \quad (13)$$

where Ω is the angular velocity in units of $^\circ/\text{Myr}$, and t is the time since impact in Myr and ϕ_0 is an initial phase offset in degrees. The bands in the similarity maps can be isolated by first ignoring all epoch-azimuth pairs with similarity scores below 0.8 and then collecting points that belong to the same diagonal band into a set. Additionally, we limit the points to times where the bands appear the most linear visually, then for each set we apply linear regression assuming the model laid out in Eqn. 13 to obtain the band's angular speed and phase offset. The parameters for the bands in arm coverage similarity has been plotted in Fig. 6.

It is clear from Fig. 6 that the pattern speed appears to increase as the average radius of the arm segments decreasing, which is unsurprising as the angular speed increases towards the centre in a differentially rotating disc.

The presence of high similarity diagonal bands for all considered arm segments (see Fig. 3 and Fig. 5) demonstrates that the simulated galaxy can achieve reasonable MW-like arm segments.

4.2 Corrugation

We construct a map of the similarity between the simulation's corrugation and the observed MW local corrugation using the method outlined in Sec. 3.4.3 which can be seen in the topmost panel of Fig. 7. We can see that the similarity starts off relatively uniform across all azimuths and is ~ 0.5 as expected since the disc is axisymmetric and stable before impact. As the perturber approaches it starts to disrupt the disc causing the similarity to drop drastically as the bending mode and breathing modes are excited, causing large scale fluctuations which tend to fit poorly. There are however still azimuths where the similarity does not change much which indicates that these exist at approximately the nodes of the oscillations where the height profile does not drastically change.

After the perturber has crossed the disc, the similarity starts to increase as the disc relaxes and flattens out. The excited bending and breathing modes are sheared by the differential rotation of the disc leading to the formation of a corrugated disc.

After about 400 Myr after impact four distinct diagonal bands of high similarity emerge. We can again model these using Eqn. 13, and through the same process of manually masking the bands and applying linear regression we were able to estimate values for the

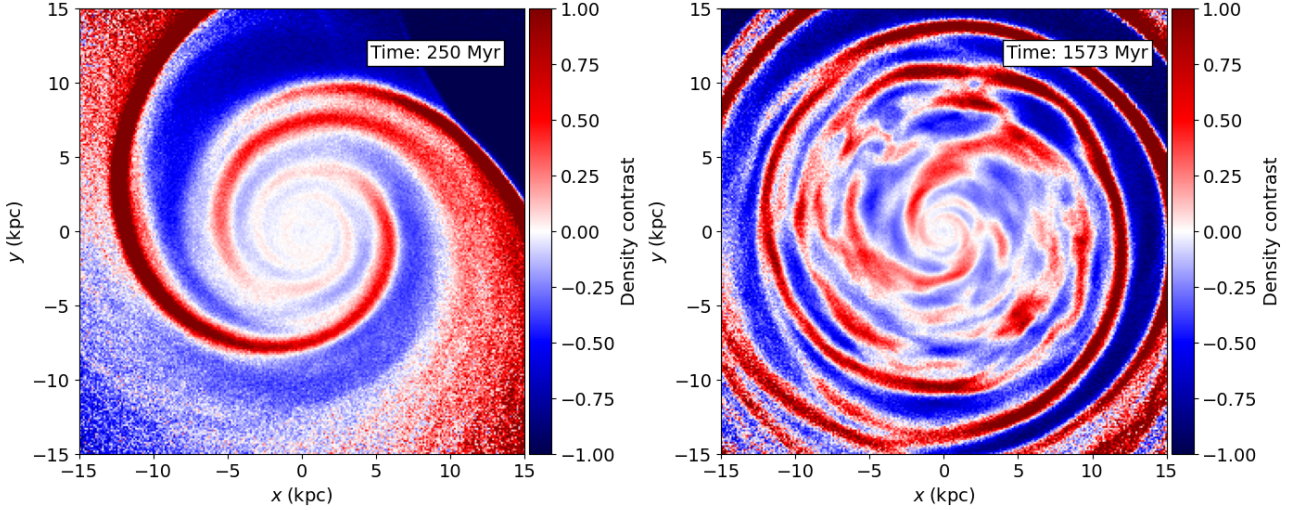


Figure 4. Two snapshots of the density contrast at two different times. Left: The density contrast at time $T = 250$ Myr where the impact has created large spanning over and underdensity regions. Right: The density contrast at a time late in the simulation where the disc has settled leading to a weakening of the spiral arms which can be seen at late times in Fig. 3.

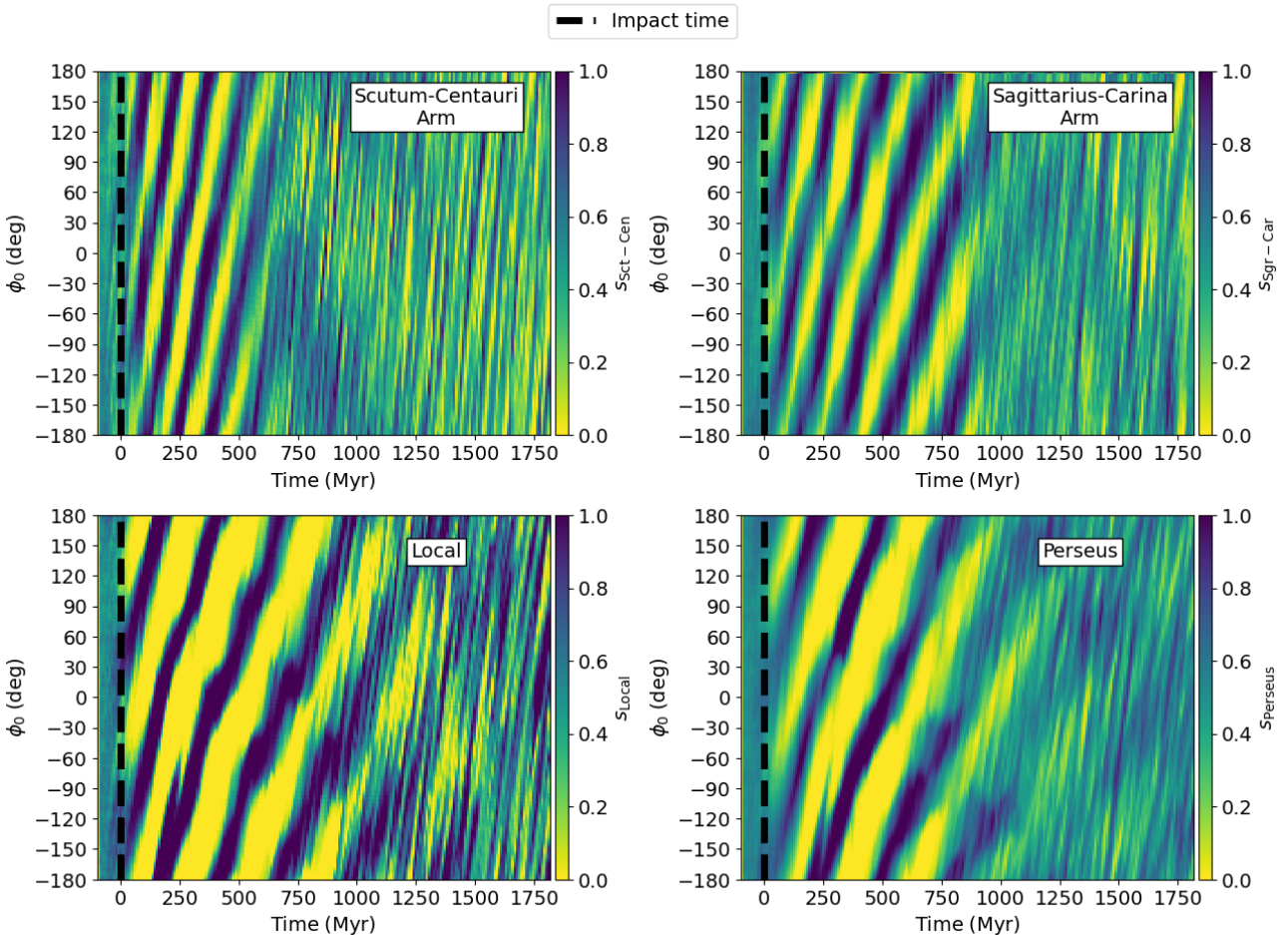


Figure 5. The arm coverage similarity over azimuth and time for the Scutum-Centauri arm (top left), Sagittarius-Carina arm (top right), Local arm (bottom left) and the Perseus arm (bottom right). In each panel, the similarity traces out two separate wrapping diagonal bands corresponding to an arm and its counter arm. These bands are highly resolved some time after the impact but eventually dissipate as the disc settles, at varying rates across arms.

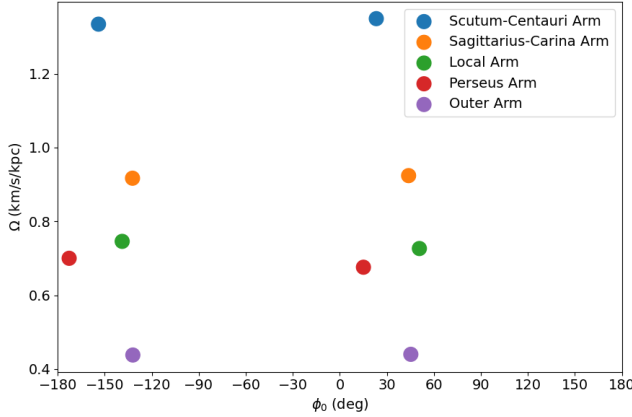


Figure 6. The fitted parameters for the diagonal bands found in arm similarity. Error bars are omitted as they are negligible at this scale.

angular velocity Ω and offsets ϕ_0 for all four bands which can be seen in Fig. 8.

The pattern speeds are similar to each other but not all of their error bars overlap. The offsets are approximately equally spaced at 90° apart forming a four-fold symmetry.

The radial wave along these bands will not be exactly static but as the bands have approximately constant similarity along it, this constrains the shape of the wave to at least be within some bounds which can be seen in Fig. 7. All four bands achieve high similarity to the observed radial wave at some point along it with values above 0.80 and have relatively bounded radial profiles.

Overall, the simulation is able to produce convincing MW-like local disc corrugations.

4.3 Estimating the impact time

As the earlier sections show, the simulation is able to produce plausibly MW-like observations of certain features at various azimuths and times; however, these features must also be consistent with each other meaning they appear MW-like at the same solar azimuth and time. Applying this constraint can lead to an estimate of the impact time of Sgr.

We apply the constraint of consistency by combining the similarity map of multiple features into a single combined similarity map by applying the following procedure:

(i) Apply a threshold to each individual similarity map to mask out poor fits, specifically, 0.5 for all residual based similarity maps like the corrugation similarity map, and 0.8 for all arm coverage based similarity maps. These values were chosen as similarity scores above 0.5 for residual based maps indicate better fits than the null model, whereas 0.8 was chosen for arm coverage based similarity maps as it effectively masks out the bands in arm coverage similarity.

(ii) Combine all the threshold similarity maps by computing their geometric mean.

The resulting similarity map is the combined threshold similarity map where non-zero values indicate where the fits for each included feature are individually above their respective chosen thresholds.

First, we will consider the similarity maps for the corrugation and the spiral arms as they fit the MW best. Both features contain high similarity bands that are well approximated by Eqn. 13 and so it is expected that in the combined similarity map, where these bands

intersect will be regions of high combined similarity. Therefore, by calculating their points of intersection, we can estimate the time after impact and azimuth where the simulation displays the MW-like features. The intersection between two bands characterised by (Ω_0, ϕ_0) and (Ω_1, ϕ_1) is given by

$$t_{\text{intersect},m} = \frac{\phi_1 - \phi_0 + 360m}{\Omega_0 - \Omega_1} \quad (14)$$

where $t_{\text{intersect},m}$ is the intersection time and m is some integer. The azimuth at that time of intersection is then simply

$$\phi_{\text{intersect},m} = \Omega_0 t_{\text{intersect},m} + \phi_0. \quad (15)$$

See Appendix C for the full derivation of Eqn. 14 and Eqn. 15, along with the equations to compute the variance of the intersection point.

Combining the Outer arm's similarity map and the corrugation similarity map results in the map shown in Fig. 9. From the map, we see that there are regions of high combined similarity near to the intersection between the high similarity bands, as suspected. The points of intersection for high combined similarity are $T = 940 \pm 20$ Myr, $\phi = 100 \pm 8^\circ$ and $T = 915 \pm 19$ Myr, $\phi = -91 \pm 8^\circ$.

As can be seen from Fig. 9, the corrugation and the Outer spiral arm do seem to appear to match well at the same time at around $T = 750 - 1200$ Myr and at two opposing sides of the disc. Assuming the corrugation and Outer arm segment in the MW are caused by an impact by Sgr, then we estimate that such an impact occurred ~ 1 Gyr ago. This is confirmed in Fig. 10 that shows the simulated galaxy at the specific azimuth and time that maximises the combined similarity.

Including the other spiral arm segments is also possible, but as each arm segment has high similarity bands with differing pattern speeds (as seen in Fig. 6), it is unlikely for all bands to intersect at a single point like in the case of two features. Although, as the bands have a non-zero width it is still possible for them to appear MW-like at the same time.

We do not find any specific azimuth and time such that all arm segments and the corrugation match well at the same time; however, after manual testing, the largest set of compatible segments are the Outer, Local, Sagittarius-Carina arms and the local disc corrugation. See Fig. 11 for a plot of the snapshot and azimuth which maximises their combined similarity. Note that the inclusion of these other arms leads to a worse match between the simulated corrugation and the observed corrugation, however, the general trend of increasing height towards outer radii is preserved.

We conclude that a Sgr-like impact, while capable of producing some MW-like spiral arms and corrugation, is unlikely to be the sole mechanism that triggered all arm segments. Specifically, the simulation does not seem to be able to reproduce the other arm segments like the Perseus arm or any of the inner spiral arm segments like the Norma arm at the same time as the other arm segments. A possible explanation is the non-linear behaviour seen at late times due to the tight-winding, inter-arm interaction.

5 DISCUSSION

5.1 Phase Spiral

The phase spiral is a clear sign of a past perturbation, and so it is not unreasonable, with hindsight, to expect spiral-like patterns to occur in the vertical phase space in our simulated galaxy, as many studies have now verified (q.v. Hunt & Vasiliev 2025). However, none of these important works considered the impact of gas. Recent work by Tepper-García et al. (2025) on this particular simulated galaxy model has shown that phase spirals are detectable from 400 Myr to

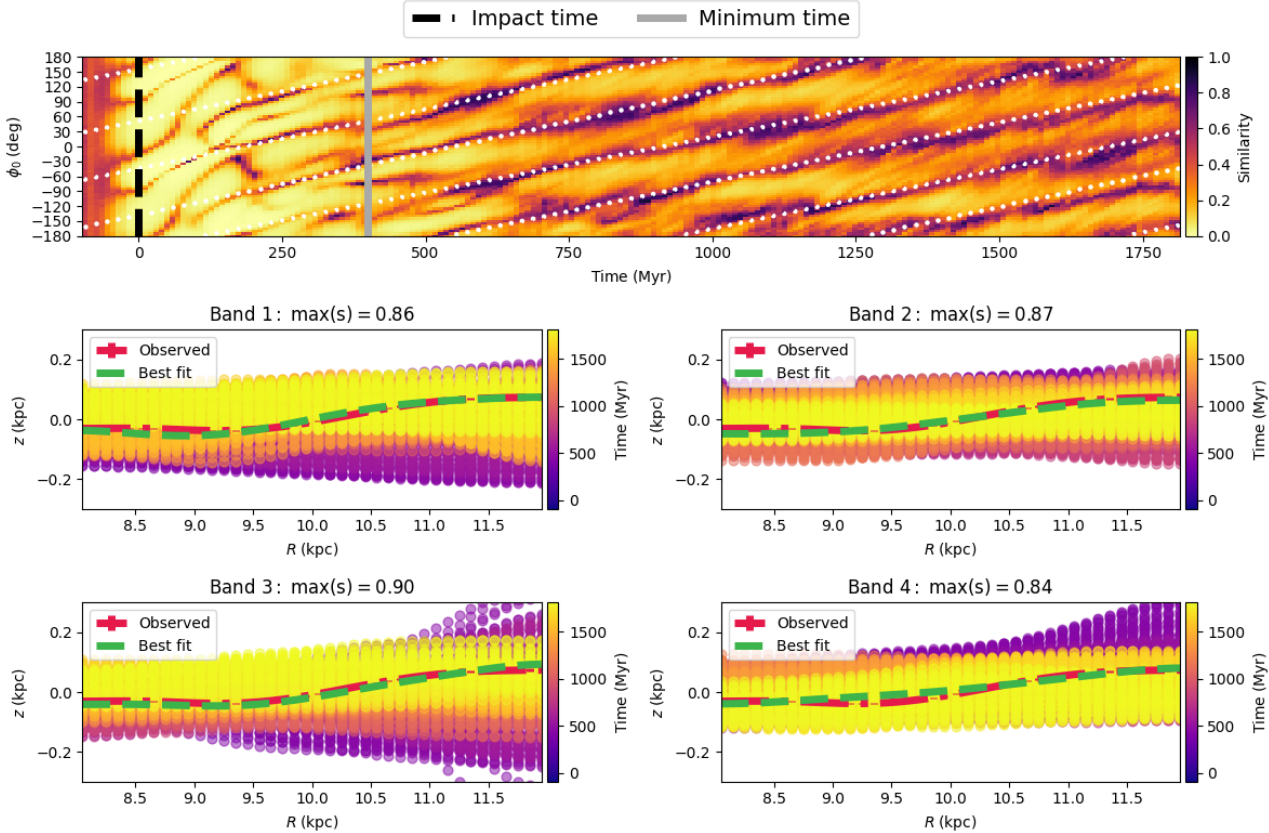


Figure 7. The top panel shows the similarity between the observed local radial height profile and the simulated radial height profile or corrugation across the solar circle for all snapshots. The time is set relative to the time of impact and the azimuth is relative to the impact's azimuth, with positive azimuths going in the anti-clockwise direction in the direction of Galactic rotation. The impact time is outlined in black. High similarity is coloured dark purple whereas low arm coverage is coloured in yellow. The similarity is structured into diagonal bands that wrap in azimuth like with arm coverage similarity. The minimum time refers to when the bands begin to appear and become linear. A fit of the diagonal bands is also overlaid on top. The bottom panels show the radial waves over time along the four bands within 5σ . The maximum similarity along the bands are also displayed on top of each panel. The time steps before the grey line at $T = 400$ Myr are ignored during the fitting process and are also not displayed in the bottom panels. The best fitting radial wave is also overlaid over the observed radial wave for each band.

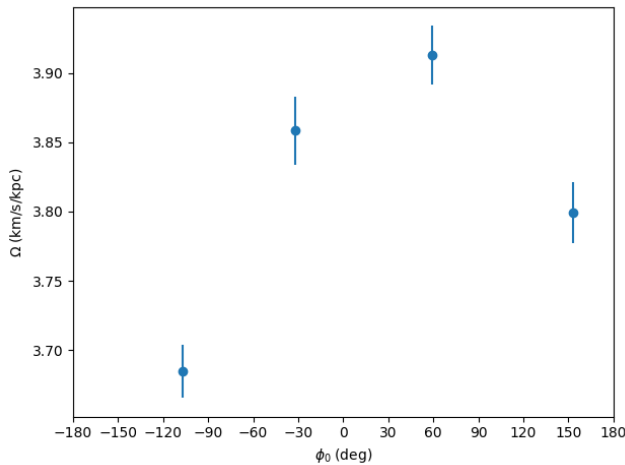


Figure 8. The fitted parameters for the four bands in the corrugation similarity map seen in Fig. 7. The error bars represent one standard deviation 1σ of uncertainty.

1200 Myr after impact. This result is consistent with the timescales of crossings between the Outer arm similarity and corrugation similarity that we found in Sec. 4.3.

Phase spirals are also present at the crossings between similarity bands as well which can be seen in the bottom panels of Fig. 10 and Fig. 11, where Fig. 10 is the epoch and azimuth that maximises the combined similarity of the Outer arm and corrugation whereas Fig. 11 maximises the combined similarity of the Local, Outer, Sagittarius-Carina arms and the corrugation. The stars comprising the phase spirals in these figures are those enclosed by a sphere of radius 1 kpc centred on each location along the solar circle.

We will defer the quantitative analysis of the degree of similarity between the simulated phase spiral and observed *Gaia* phase spiral to future work as its complex phase space structure is harder to categorise.

5.2 $L_z - \bar{V}_R$ wave

So far we have only considered the spiral arms, the corrugation and the phase spiral, extending the work of an earlier study (Bland-Hawthorn & Tepper-García 2021). But there are also other MW

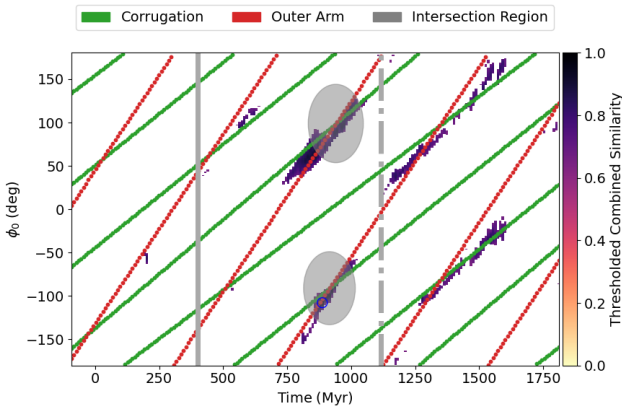


Figure 9. A plot of the threshold combined similarity of the Outer arm similarity and corrugation similarity overlaid with linear fits to each of their bands. The 5σ confidence regions corresponding to the estimated point of intersections are highlighted as grey regions. The minimum and maximum time bounds are denoted by the grey vertical lines and were decided by manual visual inspection of where the bands are most linear. The thresholded combined similarity is equal to the geometric mean of the Outer arm similarity and the corrugation similarity wherein similarities below 0.8 and 0.5 for arm similarity and corrugation similarity are respectively culled (coloured in white). Intersection regions with too few cells with high combined similarity are discarded.

features indicative of a past perturbation. The $L_z - \bar{V}_R$ wave is among many features seen in the *Gaia* data, first discovered by Friske & Schönrich (2019). It appears as an in-plane wave pattern in the mean radial velocity $\langle V_R \rangle$ when binned in angular momentum L_z . Like the other features discussed, we suspect this pattern is a signal, at least in part, of a past perturbation.

We sample a sphere centred on the Sun of radius 2 kpc and then bin in angular momentum from 1200 kpc km s $^{-1}$ to 2600 kpc km s $^{-1}$; we then calculate the mean radial velocity of the stars in each bin. The observed sample is from *Gaia* DR2 using the same cuts used by Friske & Schönrich (2019).

We attempted to find an epoch-azimuth pair that agreed well with the observed $L_z - \bar{V}_R$ wave using residual-based similarity (previously used to quantify corrugation similarity). Fig. 12 shows our similarity map for the $L_z - \bar{V}_R$ wave and it clearly lacks the bands of high similarity found in the spiral arms and corrugation maps. Thus, for this diagnostic, we fail to find a convincing match.

This similarity map is very different when compared to the corrugation and spiral arm maps. Rather than correlated band features, we see regions of low and medium similarity instead. The simulation does not produce any reasonably MW-like waves in $L_z - \bar{V}_R$ space except stochastically at late times, $T > 1250$ Myr, with the similarity averaging around 0.2. The $L_z - \bar{V}_R$ projection at the crossings shown in Fig. 10 and Fig. 11 in the top right panels is also not convincingly MW-like, with structural differences in the simulated (green) pattern compared to the observed pattern (red).

This can be attributed to the more complex structure of the observed $L_z - \bar{V}_R$ wave that contains at least two dominant wave components compared to the one wave component of the corrugation with shorter wavelengths relative to the observed window. Additionally, previous work by Bernet et al. (2025) predicts that the amplitude ratio between the fast and slow waves in the $L_z - \bar{V}_R$ signature does not support a satellite impact origin, but rather points towards an internal mechanism. Cao et al. (2024) also show evidence against an

external cause as well. Hence, it seems unlikely the $L_z - \bar{V}_R$ wave originates from a single Sgr-like impact as confirmed by our results.

5.3 Inclusion of Gas

The simulated galaxy model so far lacks important physics, e.g., the presence of a gaseous component. In the following section, we explore how adding inert gas and star-forming gas can affect the formation of structures by applying the same methodology as described earlier to these models (q.v. Tepper-García et al. 2024).

The model studied so far has been a pure N-body realisation. As Tepper-García et al. (2025) shows, the inclusion of gas can greatly influence the evolution and formation of features such as the phase spiral, hence it is also important to consider its effects here. The following sections will explore two more models which include gas and more realistic physics and see how these extra inclusions affect the similarity.

5.3.1 Inert Gas Model

We will be utilising an inert isothermal gas galaxy model first presented in Tepper-García et al. (2022). This model is exactly the same as the model used above; however, there is an added component comprising an inert isothermal gas, distributed as an exponential disc with scale length $R_d = 6$ kpc with mass $M_{\text{gas}} \approx 4 \times 10^9 M_{\odot}$, with a 10% gas fraction relative to the total disc mass. The gas is evolved via a strict isothermal equation of state with temperature $T = 10^3$ K and is thus inert. See Sec. 2 of Tepper-García et al. (2025) for a more in-depth explanation of the model’s parameters and setup labelled *fg10_nsf*.

We apply the same methods as laid out in Sec. 3 to these models to plot the combined similarity map of the Outer arm similarity and corrugation similarity to produce Fig. 13. As compared to the gasless model, the regions are much larger due to the increased uncertainty in the fitted parameters. This is a result of the model increasing the noise in the similarity maps making the bands hazier. Overall, the inclusion of an inert gas disc appears to reduce the times and azimuths where multiple features match well at the same time.

A plot of the best fit epoch and azimuth for the inert gas model is also presented in Fig. 14. It is apparent from the top left panel that the spiral arms are much more flocculent than in the pure N-body case presented in Fig. 10 and Fig. 11. The phase spirals in the bottom panels are also much weaker in comparison. Finally, the projection $L_z - \bar{V}_R$ does not match the observations at all.

5.3.2 Star Forming Gas Model

In the previous section we included a gas disc; however, that gas was isothermal and inert, therefore, we have not included any form of stellar feedback or turbulence. In this section, we now introduce multi-phase gas that can undergo star formation leading to stellar feedback. The model we will studying was first presented in Tepper-García et al. (2025), specifically, the *fg20_sf* model which in addition to the stellar components of the pure N-body model also includes a gas disc with mass equal to 20% of the total disc mass, so $M_{\text{gas}} \approx 9 \times 10^9 M_{\odot}$ and with an initial temperature of $T = 2 \times 10^3$ K. We refer the reader to Sec. 2 of Tepper-García et al. (2025) for a more in-depth explanation of the simulation parameters.

As the gas can now form stars, this creates a distinction between stars that are pre-existing and stars that are newly formed. In order to

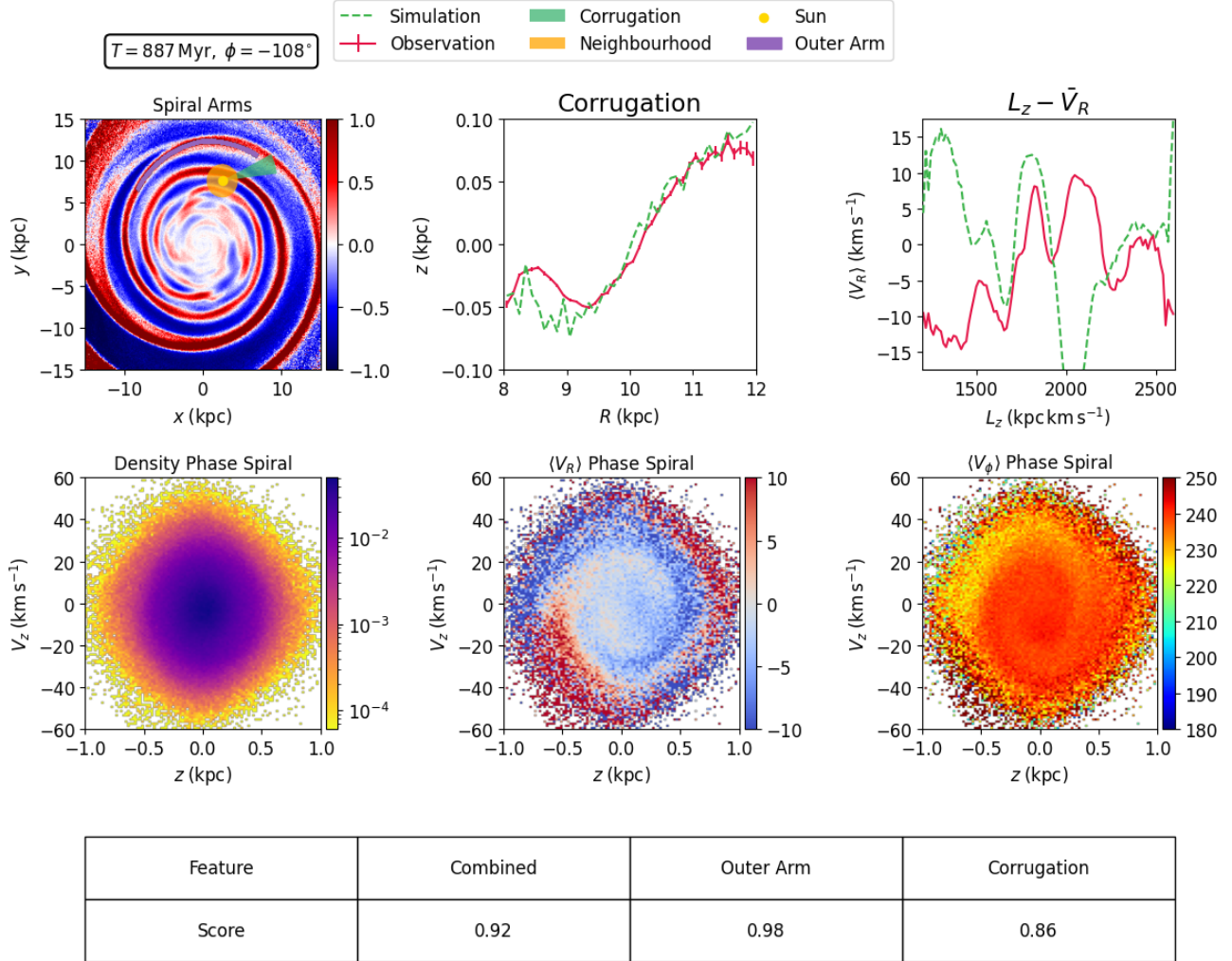


Figure 10. Top left: Density contrast map of the simulated disc galaxy. The model Outer arm is overlaid in purple, the Sun’s position is marked in yellow, the neighbourhood used for the phase spiral is shaded in yellow, and the region used to extract the corrugation profile is shown in green. Top middle: Radial height profile of the disc corrugation, comparing the observed MW profile (red) with the simulated profile (green). Top right: The mean radial velocity binned in angular momentum or the $L_z - \bar{V}_R$ wave, comparing the observed MW profile (red) with the simulated profile (green). Bottom left: The simulated vertical phase space distribution seen in surface number density. Bottom middle: The simulated vertical phase space distribution seen in mean radial velocity (in units of km s^{-1}). Bottom right: The simulated vertical phase space distribution seen in mean azimuthal velocity (in units of km s^{-1}). All non-observational data correspond to the simulation snapshot at $T = 887$ Myr and solar azimuth $\phi = -108^\circ$, the configuration that maximises the combined similarity score of the Outer arm and corrugation. A table of the similarity scores for the Outer arm and corrugation is located below the panels.

keep the comparisons fair, we elect to only consider the pre-existing stars in this study.

We apply the same methods as in Sec. 5.3.1 to obtain an intersection plot showcasing the combined similarity of the Outer arm and corrugation which can be seen in Fig. 15. Although the regions are more constrained, they contain less cells with non-zero threshold combined similarity compared to previous models. The introduction of feedback increases the speed of decoherence in the spiral arms, and the added energy causes the radial wave oscillations to be messier, resulting in even more flocculent similarity maps.

The plot of the best fit epoch and azimuth pair for this model considering only the combined similarity of the Outer arm and corrugation is shown in Fig. 16. Like with the inert gas model, the density contrast plot in the top left panel shows a more flocculent spiral structure than even Fig. 14. The $L_z - \bar{V}_R$ projection is even

worse of a match than before, and the phase spirals are incredibly weak. Although the corrugation appears to match somewhat as a general trend, that is, it starts slightly negative and then increases until it plateaus around $R = 10 - 11$ kpc, it has a less smooth profile. This is likely due to the increased turbulence from stellar feedback from the active gas disc.

5.3.3 Result of Including Gas

As explained by [Tepper-García et al. \(2025\)](#), the inclusion of additional gas serves to introduce a few effects:

- (i) Increase in mass - As the stellar components are kept identical between the models, the inclusion of gas increases the total mass of

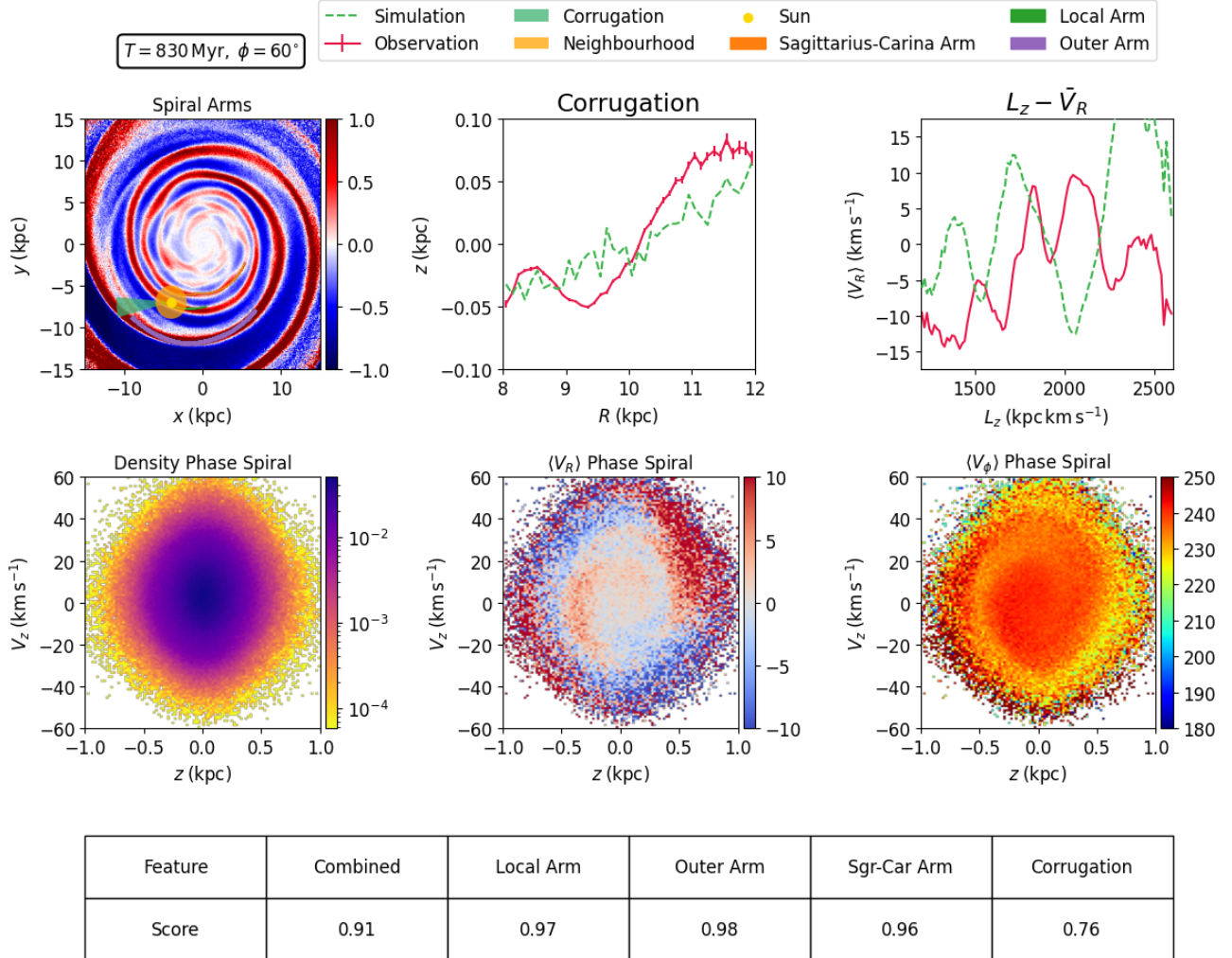


Figure 11. Top left: Density contrast map of the simulated disc galaxy. The model Outer arm is overlaid in purple, the model Local arm is coloured in green, the model Sagittarius-Carina arm is in orange, the Sun’s position is marked in yellow, the neighbourhood used for the phase spiral is shaded in yellow and the region used to extract the corrugation profile is shown in green. Top middle: Radial height profile of the disc corrugation, comparing the observed MW profile (red) with the simulated profile (green). Top right: The mean radial velocity binned in angular momentum or the $L_z - \bar{V}_R$ wave, comparing the observed MW profile (red) with the simulated profile (green). Bottom left: The simulated vertical phase space distribution seen in surface number density. Bottom middle: The simulated vertical phase space distribution seen in mean radial velocity (in units of km s^{-1}). Bottom right: The simulated vertical phase space distribution seen in mean azimuthal velocity (in units of km s^{-1}). All non-observational data correspond to the simulation snapshot at $T = 830$ Myr and solar azimuth $\phi = 60^\circ$, the configuration that maximises the combined similarity score of the Outer arm, Local arm, Sagittarius-Carina arm and corrugation. A table of the similarity scores for the corrugation and the chosen spiral arms is located below the panels.

the system. This decreases the responsiveness of the galaxy to the external perturber which is kept at the same mass.

(ii) The speeding up of phase-mixing - The gas component will increase the rate of phase mixing, which along with negatively impacting phase spirals, also increases the rate of spiral density wave decoherence. This is clear in Fig. 17 where the gas models have much more flocculent spiral arms compared to the pure N-body model at approximately the same time in the simulation.

Therefore, it seems with our current models, the inclusion of gaseous components and feedback hinder the match between simulations and observations. This suggests several possibilities: (i) the gas phase may need magnetohydrodynamics (MHD) to help soften the previously mentioned effects, or (ii) that the self-gravity between stars is the more dominant force compared to star-gas interactions,

and that the feedback in the studied models is too strong. In this respect, the sensitivity of the phase spiral to the noise means that it can be used to constrain feedback prescriptions.

6 CONCLUSIONS

In this study, we proposed a null hypothesis - that a single crossing event can plausibly be the dominant origin of specific MW substructures. As the number of possible signatures is increased, we find that the hypothesis must be rejected.

We analysed primarily a pure N-body simulation first presented by Bland-Hawthorn & Tepper-García (2021) consisting of a thin MW-like disc and a disc-crossing point mass perturber mimicking the

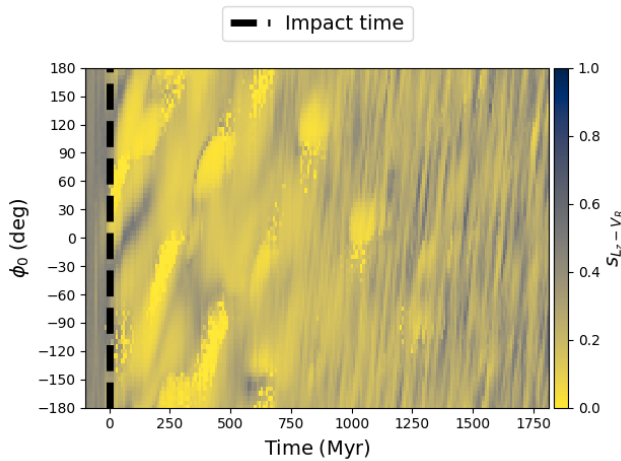


Figure 12. The similarity of the $L_z - \bar{V}_R$ wave as a function of azimuth and time where time is set relative to the time of impact and the azimuth is relative to the impact's azimuth, with positive azimuths going in the anti-clockwise direction. There are distinct regions of low similarity (coloured in yellow).

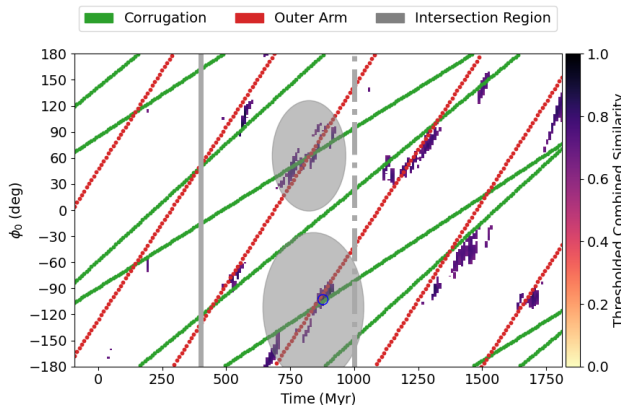


Figure 13. Same plot as in Fig. 9 but of the inert isothermal gas galaxy model. The blue circle corresponds to the best matching time and azimuth with respect to the combined similarity of the Outer arm and corrugation.

interaction between the MW and the Sgr dwarf galaxy. We also analysed more sophisticated galaxy models that included either an inert gas disc component or a star-forming, turbulent gas disc component. Here are the main findings:

- (i) A single impact is able to produce MW-like disc corrugations and a MW-like Outer arm approximately 700–1200 Myr after crossing at two opposing sides of the galaxy for all three models.
- (ii) The present simulations are not able to produce arm segments that match well with all observed MW spiral arm segments at the same azimuth and time. This is because each arm segment has its own pattern speed, as seen in their similarity maps, making it unlikely for multiple arms to match observations at the same point along the solar circle and in time.
- (iii) The largest compatible set of features are the MW Outer arm, Local arm and Sagittarius-Carina arm and the local disc corrugation. Additionally, the phase spiral is also qualitatively detectable along with these features.

(iv) The $L_z - \bar{V}_R$ wave signature in our simulations does not appear to match well with observation, indicating that a single Sgr-like impact may not be responsible for this phenomena. This is in line with other studies that lean towards a more internal origin.

(v) Including gas appears to worsen the comparison to observation likely due to the increased mass dampening the effect of the satellite's perturbation and also due to star-gas interactions serving to decohere structures over time.

(vi) Inner disc structures such as the Norma and Scutum-Centauri arm segments are not well reproduced in the simulations, likely due to the lack of a bar.

(vii) Overall, a single impact by a satellite like Sagittarius cannot account for all disc substructures in the Galaxy. Future models will need to include a more sophisticated treatment of the gas, with a close examination of the non-linearity of bar-spiral arm interaction (Minchev et al. 2012), *inter alia*.

ACKNOWLEDGEMENTS

We would like to thank Austin Hinkel for their assistance and clarifications on the query and cuts used to obtain the local corrugation profile. We are also grateful to Mark Reid for their help with regard to observational spiral arm data.

DATA AVAILABILITY

The data associated with this article is available to be shared on request.

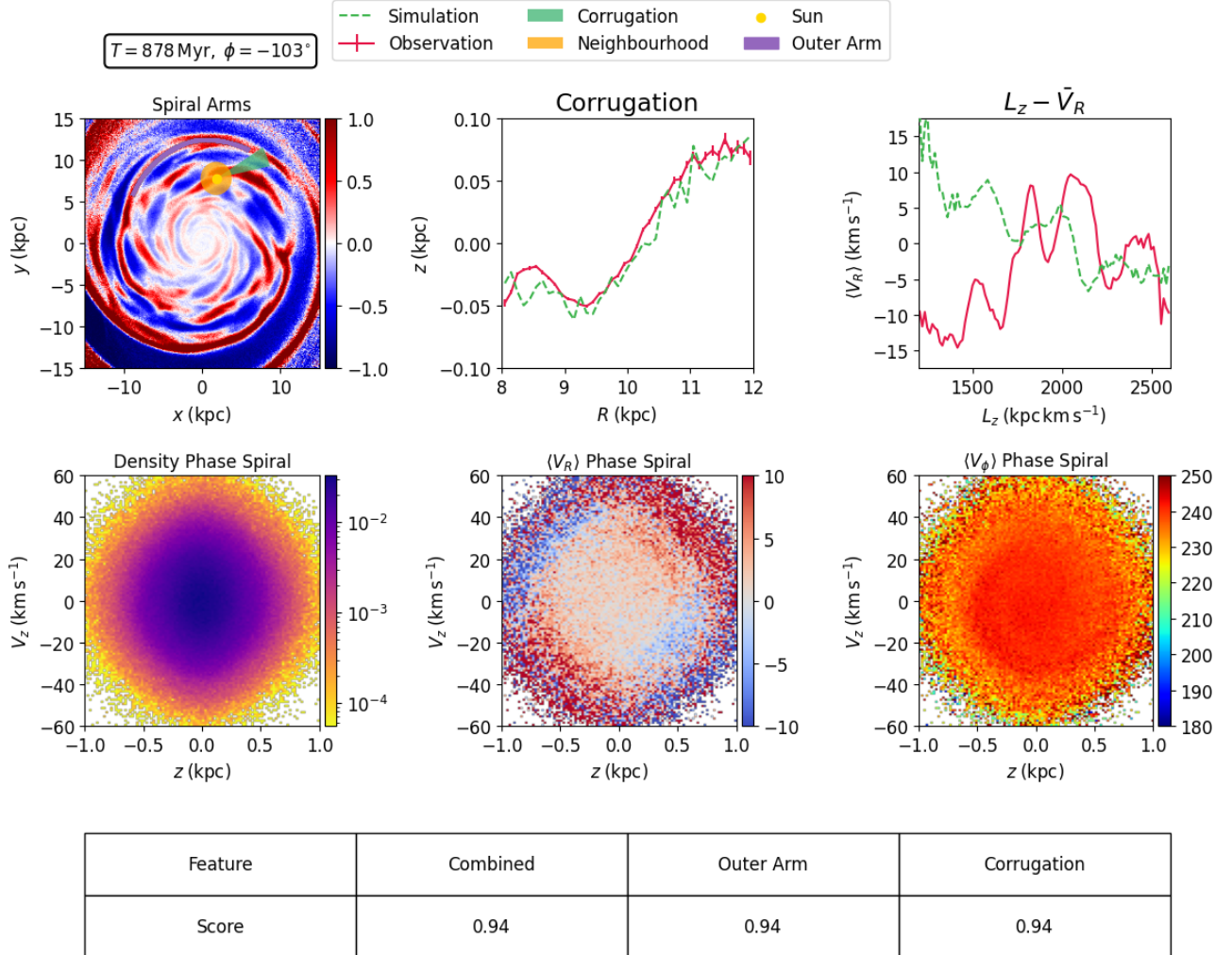


Figure 14. Top left: Density contrast map of the simulated disc galaxy with an **inert** gas disc. The model Outer arm is overlaid in purple, the Sun’s position is marked in yellow, the neighbourhood used for the phase spiral is shaded in yellow, and the region used to extract the corrugation profile is shown in green. Top middle: Radial height profile of the disc corrugation, comparing the observed MW profile (red) with the simulated profile (green). Top right: The mean radial velocity binned in angular momentum or the $L_z - \bar{V}_R$ wave, comparing the observed MW profile (red) with the simulated profile (green). Bottom left: The simulated vertical phase space distribution seen in surface number density. Bottom middle: The simulated vertical phase space distribution seen in mean radial velocity (in units of km s^{-1}). Bottom right: The simulated vertical phase space distribution seen in mean azimuthal velocity (in units of km s^{-1}). All non-observational data correspond to the simulation snapshot at $T = 878$ Myr and solar azimuth $\phi = -103^\circ$, the configuration that maximises the combined similarity score of the Outer arm and corrugation. A table of the similarity scores for the corrugation and the Outer arm is located below the panels.

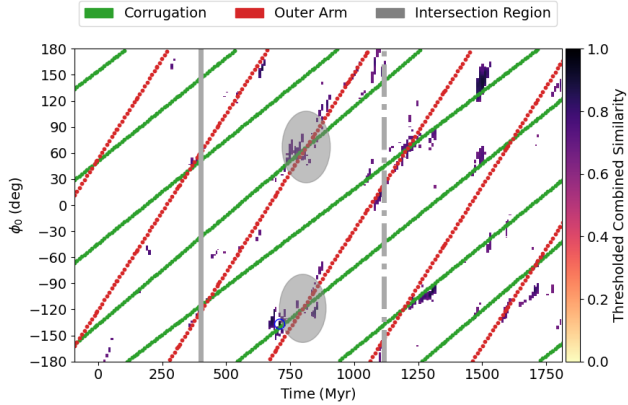


Figure 15. Same plot as in Fig. 9 but of the multi-phase star forming gas galaxy model. The blue circle corresponds to the best matching time and azimuth with respect to the combined similarity of the Outer arm and corrugation.

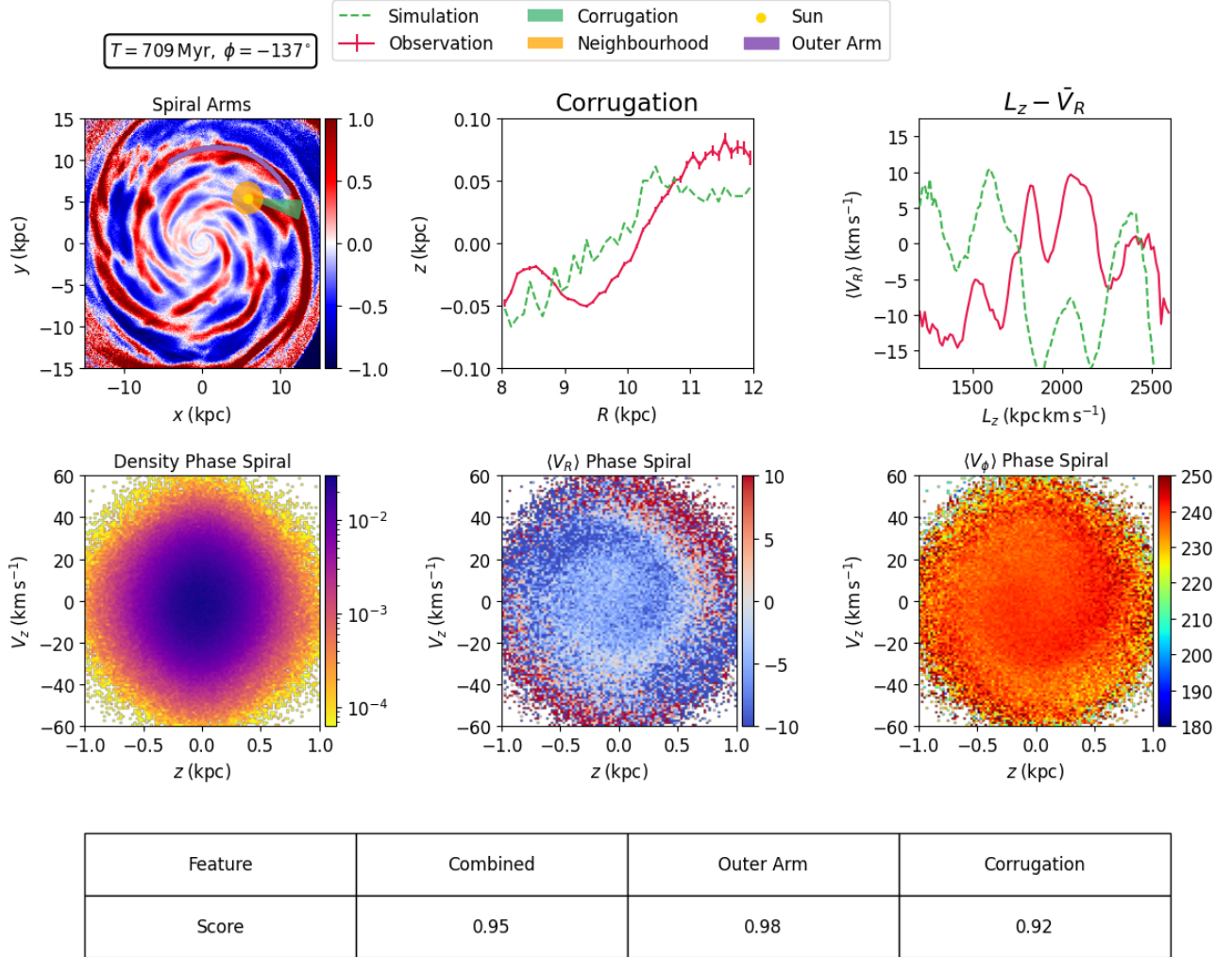


Figure 16. Top left: Density contrast map of the simulated disc galaxy with an **active** gas disc. The model Outer arm is overlaid in purple, the Sun’s position is marked in yellow, the neighbourhood used for the phase spiral is shaded in yellow, and the region used to extract the corrugation profile is shown in green. Top middle: Radial height profile of the disc corrugation, comparing the observed MW profile (red) with the simulated profile (green). Top right: The mean radial velocity binned in angular momentum or the $L_z - \bar{V}_R$ wave, comparing the observed MW profile (red) with the simulated profile (green). Bottom left: The simulated vertical phase space distribution seen in surface number density. Bottom middle: The simulated vertical phase space distribution seen in mean radial velocity (in units of km s^{-1}). Bottom right: The simulated vertical phase space distribution seen in mean azimuthal velocity (in units of km s^{-1}). All non-observational data correspond to the simulation snapshot at $T = 708$ Myr and solar azimuth $\phi = -137^\circ$, the configuration that maximises the combined similarity score of the Outer arm and corrugation. A table of the similarity scores for the corrugation and the Outer arm is located below the panels.

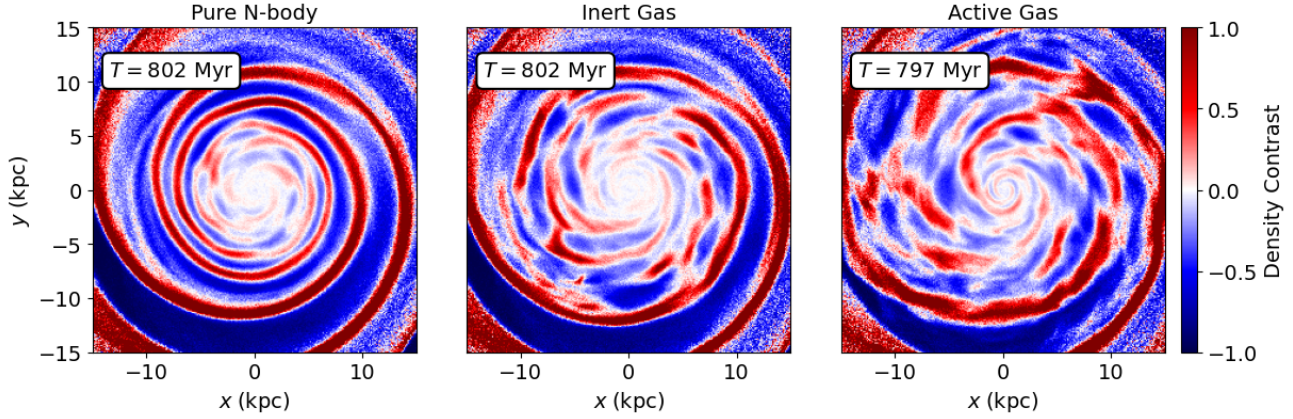


Figure 17. A comparison between the density contrast of Sgr impact models at approximately the same amount of time after the perturber's impact, ~ 800 Myr. The leftmost panel is of the pure N-body model, the middle panel is of the inert gas model and the rightmost panel is of the star forming gas model. It is clear that including gas and then also including stellar formation leads to more flocculent spirals.

REFERENCES

Agertz O., et al., 2021, *MNRAS*, 503, 5826
 Antoja T., et al., 2018, *Nature*, 561, 360
 Antoja T., Ramos P., López-Guitart F., Anders F., Bernet M., Laporte C. F. P., 2022, *A&A*, 668, A61
 Bennett M., Bovy J., 2019, *MNRAS*, 482, 1417
 Bernet M., Ramos P., Antoja T., Price-Whelan A., Brunton S. L., Asano T., Girón-Soto A., 2025, *arXiv e-prints*, p. arXiv:2506.17383
 Binney J., Schönrich R., 2018, *Monthly Notices of the Royal Astronomical Society*, 481, 1501
 Bland-Hawthorn J., Tepper-García T., 2021, *Monthly Notices of the Royal Astronomical Society*, 504, 3168
 Bland-Hawthorn J., et al., 2019, *MNRAS*, 486, 1167
 Bland-Hawthorn J., Tepper-García T., Agertz O., Freeman K., 2023, *ApJ*, 947, 80
 Cao C., Li Z.-Y., Schönrich R., Antoja T., 2024, *ApJ*, 975, 292
 Friske J. K. S., Schönrich R., 2019, *MNRAS*, 490, 5414
 Fujii M. S., Bédorf J., Baba J., Portegies Zwart S., 2018, *MNRAS*, 477, 1451
 Grand R. J. J., Pakmor R., Fragkoudi F., Gómez F. A., Trick W., Simpson C. M., van de Voort F., Bieri R., 2023, *MNRAS*, 524, 801
 Hey D. R., et al., 2023, *The Astronomical Journal*, 166, 249
 Hunt J. A. S., Vasiliev E., 2025, *New Astron. Rev.*, 100, 101721
 Khoperskov S., Di Matteo P., Gerhard O., Katz D., Haywood M., Combes F. o., Berczik P., Gomez A., 2019, *A&A*, 622, L6
 Lin C. C., Shu F. H., 1964, *ApJ*, 140, 646
 Lynden-Bell D., 1967, *MNRAS*, 136, 101
 Minchev I., Famaey B., Quillen A. C., Di Matteo P., Combes F., Vlajić M., Erwin P., Bland-Hawthorn J., 2012, *A&A*, 548, A126
 Monari G., Kawata D., Hunt J. A. S., Famaey B., 2017, *MNRAS*, 466, L113
 Poggio E., et al., 2021, *A&A*, 651, A104
 Poggio E., et al., 2025, *A&A*, 699, A199
 Purcell C. W., Bullock J. S., Tollerud E. J., Rocha M., Chakrabarti S., 2011, *Nature*, 477, 301
 Reid M. J., et al., 2014, *ApJ*, 783, 130
 Reid M. J., et al., 2019, *The Astrophysical Journal*, 885, 131
 Schönrich R., Dehnen W., 2018, *MNRAS*, 478, 3809
 Sellwood J. A., Carlberg R. G., 1984, *ApJ*, 282, 61
 Sellwood J. A., Carlberg R. G., 2022, *MNRAS*, 517, 2610
 Söding L., et al., 2025, *A&A*, 693, A139
 Tepper-García T., et al., 2021, *arXiv e-prints*, p. arXiv:2111.05466
 Tepper-García T., Bland-Hawthorn J., Freeman K., 2022, *MNRAS*, 515, 5951
 Tepper-García T., Bland-Hawthorn J., Vasiliev E., Agertz O., Teyssier R., Federrath C., 2024, *MNRAS*, 535, 187
 Tepper-García T., Bland-Hawthorn J., Bedding T. R., Federrath C., Agertz O., 2025, *MNRAS*, 542, 1987
 Teyssier R., 2002, *A&A*, 385, 337
 Tremaine S., Frankel N., Bovy J., 2023, *MNRAS*, 521, 114
 Vasiliev E., 2019, *MNRAS*, 482, 1525
 Widrow L. M., Gardner S., Yanny B., Dodelson S., Chen H.-Y., 2012, *ApJ*, 750, L41
 Yin Z., Hinkel A., 2024, *The Astrophysical Journal*, 963, 136

APPENDIX A: SPIRAL ARM TOY MODEL AND SIMILARITY MAPS

In order to better understand the similarity map for the spiral arms, let us first consider a simple toy model. In this toy model we will assume the galaxy has two spiral arms in the shape of two log spirals, one arm and its counter arm 180 degrees away.

In the ideal case where the mask arm (the observed arm we are comparing to) is identical to the two spiral arms (the simulated arms we are matching with observation) we expect that the coverage will peak to 100% only when the mask's azimuths is equal to the azimuths of the two spiral arms as any other angle will leave cells missing,

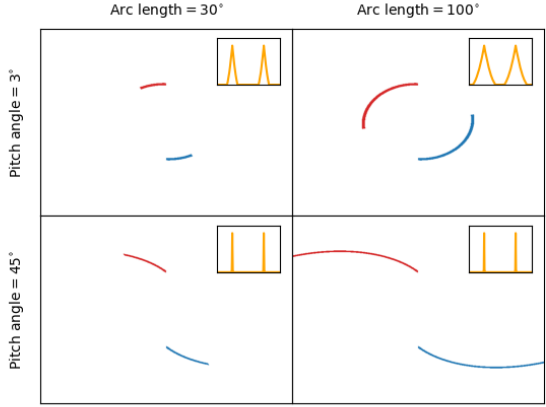


Figure A1. Each panel shows an arm and its counter-arm in red and blue along with a plot of its coverage with respect to an identical mask arm for angles between -180° and $+180^\circ$ in the top right. The top row shows arms with pitch angle 3° whereas the bottom row shows arms with a larger pitch angle 45° . The left column corresponds to arms with short arc lengths of 30° while the right column corresponds to long arc lengths of 100° . It can be seen that the width of the peaks is much smaller in the case of high pitch angles (bottom panels) as compared to lower pitch angles (top panels).

ignoring any potential discretisation errors. The width over which the coverage is non-zero is dependent on the exact shape of the spiral as the more non-circular it becomes the more difficult it is for the mask to fit to the spiral arms at non-optimal angles. See Fig. A1 for examples of some configurations and their coverage profiles.

In the non-ideal cases where the mask arm differs from the underlying spiral arms, we can expect the peaks to lower and potentially shift. Additionally if the spiral arms were modelled instead with kinked log spirals (like in the models presented by Reid et al. (2019)), depending on the exact configuration of the kink, the peaks may even become lopsided.

Under constant angular rotation, these peaks will travel with the same angular velocity as the arms forming diagonal bands where the gradient is equal to the angular velocity. As all the rotation does is impart a constant global azimuthal offset, the shapes of the peaks will not change over time and so the diagonal bands will only have straight edges, as can be seen in Fig. A2.

An issue with the coverage method is that having 100% coverage does not always mean that the mask arm fits well. Any ring-like structure that covers all azimuths and has a larger area than the mask can lead to a coverage profile that is uniformly at 100% coverage even though such a ring structure is nothing like the mask arm. See Fig. A3 for an illustration.

Therefore, it is important that we see peaks and troughs in the coverage profile as that better indicates the presence of arm segments.

APPENDIX B: SENSITIVITY OF RESIDUAL-BASED SIMILARITY

The method to quantify similarity for the corrugation that used the sum of square residuals approach is more sensitive to small changes in the frequency/structure of a signal than it is to small changes in amplitude.

Let's consider an example. The observed MW corrugation radial

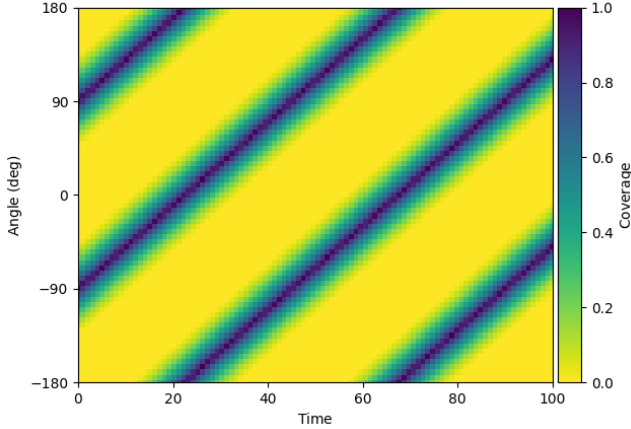


Figure A2. The coverage over time and azimuth for a system with an arm and its counter arm rotating at a constant angular velocity. The coverage peaks where the arms are located and their rotation leads to wrapping diagonal bands over time.

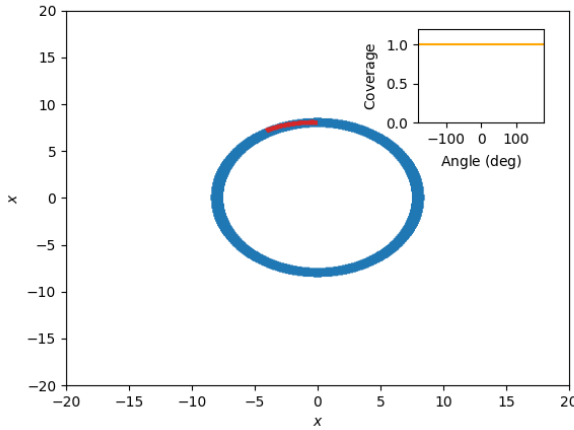


Figure A3. The degenerate case where the overdensity map contains a ring structure that encompasses the entirety of the mask arm leading to complete coverage over all azimuths.

wave can be modelled roughly as a single sine wave of the form

$$z(R) = A \sin(\omega R + \phi_0) + z_0 \quad (\text{B1})$$

where z is the height, A is the amplitude, ω is the wave frequency, R is the radius, ϕ_0 is its phase and z_0 is the height at $R = 0$ or offset. We can imagine a slightly perturbed version of this wave to be

$$z'(R) = A' \sin(\omega' R + \phi'_0) + z'_0 \quad (\text{B2})$$

where all parameters are slightly perturbed. We can quantify this

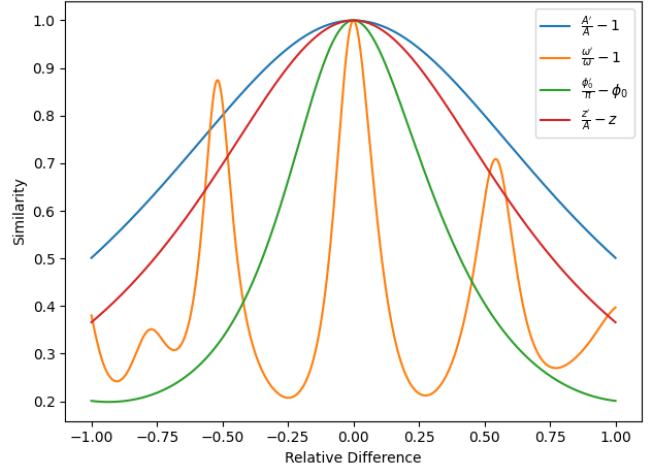


Figure B1. The similarity as the amplitude, wave frequency, phase and offset are perturbed.

perturbation as a relative or normalised difference in parameters

$$a = \frac{A'}{A} \quad (\text{B3})$$

$$w = \frac{\omega'}{\omega} \quad (\text{B4})$$

$$\Phi = \frac{\phi'_0}{\pi} \quad (\text{B5})$$

$$Z = \frac{z'_0}{A} \quad (\text{B6})$$

where the amplitude and wave frequency are relative to the true values, and the phase and offset are relative to π radians and the amplitude respectively.

We can then measure how the similarity changes as a result of changing these parameters, using the null model of a flat profile with height 0. As can be seen from Fig. B1, amplitude does not cause much of a change in similarity from 0 to 2 times the original amplitude, whereas even a small change in wave frequency can lead to a large drop in similarity. The phase and offset are also more sensitive than the amplitude which indicates that similarity is more sensitive to changes in the structure of a signal than it is in the amplitude. This effect leads to more pessimistic estimations of the similarity for features which are more complicated in structure like $L_z - \bar{V}_R$ and the 2D phase spiral signature.

APPENDIX C: DERIVATION OF INTERSECTION POINT BETWEEN TWO PERIODICALLY WRAPPING LINES

The lines cross when their azimuths match which with 360° periodicity means

$$\Omega_0 t + \phi_0 \equiv \Omega_1 + \phi_1 \pmod{360} \quad (\text{C1})$$

where (Ω_i, ϕ_i) are the angular velocity and initial offset for line $i = 0, 1$. If we write it in non-modular arithmetic notation we get

$$\Omega_0 t + \phi_0 - \Omega_1 t - \phi_1 = 360m \quad (\text{C2})$$

where m is some integer. Solving for time t we get

$$t_{\text{intersect},m} = \frac{\phi_1 - \phi_0 + 360m}{\Omega_0 - \Omega_1} \quad (\text{C3})$$

Substituting Eqn. C3 into Eqn. 13 we get the azimuth at intersection as well

$$\phi_{\text{intersect},m} = \Omega_0 \left(\frac{\phi_1 - \phi_0 + 360m}{\Omega_0 - \Omega_1} \right) + \phi_0 \quad (\text{C4})$$

The variance of both coordinates can be obtained through the usual uncertainty propagation rules.

The variance, σ_t of t is given by

$$\sigma_t^2 = \frac{1}{b^2} \left(\sigma_{\phi_0}^2 + \sigma_{\phi_1}^2 \right) + \frac{a^2}{b^4} \left(\sigma_{\Omega_0}^2 + \sigma_{\Omega_1}^2 \right) \quad (\text{C5})$$

and the variance of ϕ is

$$\sigma_\phi^2 = \frac{\Omega_1^2}{b^2} \sigma_{\phi_0}^2 + \frac{\Omega_0^2}{b^2} \sigma_{\phi_1}^2 + \frac{a^2 \Omega_1^2}{b^4} \sigma_{\Omega_0}^2 + \frac{a^2 \Omega_0^2}{b^4} \sigma_{\Omega_1}^2 \quad (\text{C6})$$

where $a = \phi_1 - \phi_0 + 360m$ and $b = \Omega_0 - \Omega_1$.

This paper has been typeset from a $\text{\TeX}/\text{\LaTeX}$ file prepared by the author.